Pure Appl. Geophys.
© 2022 The Author(s)
https://doi.org/10.1007/s00024-022-03071-3

Pure and Applied Geophysics

Exploration of a Copper Ore Deposit in Elbistan/Turkey Using 2D Inversion of the Time-Domain Induced Polarization Data by Using Unstructured Mesh

Juliane Adrian,[1,2] Bülent Tezkan,[1] and M. Emin Candansayar[3]

Abstract—We present the results of a direct current (DC) resistivity and time-domain induced polarization (TDIP) survey exploring a copper ore deposit in Elbistan/Turkey. The ore deposit is elongated below a valley and is of disseminated form with sulfide content. DC and IP data were acquired using the pole-dipole array on eight parallel profiles crossing the valley perpendicularly. The length of each profile was 300 m with an inter-profile distance of about 50 m. The data were interpreted by a newly developed 2D DC/TDIP inversion algorithm. The finite element algorithm uses a local smoothness constrained regularization on unstructured meshes. The finite element forward solution, as well as the inverse problem, is solved by an iterative preconditioned conjugate solver. The depth of investigation (DOI) was determined from cumulative sensitivities of the 2D inversion algorithm results. Because of the dissemination of the ore, the 2D inversion of the DC data was ambiguous: However, due to the sulfide content, a strong chargeability anomaly associated with the ore body was detected. We show that chargeability anomalies can generally be detected in the absence or presence of corresponding resistivity anomalies. This highly chargeable structure was confined in lateral direction. Although the lower boundary of the structure could not be resolved by the applied field set-up, a rough estimation of it could be derived at a depth of 90 m using synthetic modeling analyses. The 2D chargeability models are consistent with existing borehole information.

Keywords: Ore exploration, direct current resistivity, induced polarization, 2D inversion, finite elements.

1. Introduction

Mineral exploration is an important task that serves to investigate the characteristics, such as size and shape, of a mineral deposit prior to the exploitation. The application of geophysical methods serves the non-destructive characterization of the subsurface. If applied, covering a large area, it is a powerful tool to define outlines of a potential mineral deposit and suggests promising locations for boreholes or excavations. In mineral exploration, the direct current (DC) resistivity method is commonly combined with the induced polarization (IP) method (Pelton et al., 1978). The advantage of using IP in addition to pure DC is that the resistivity signature caused by disseminated material is hard to detect whereas the chargeability signature resolved by the IP method might be strong and rather independent from the geometry of the resistivity structure. In this case, the DC method gives an overview of the general geology while the IP method provides information about a potential ore deposit (Spitzer & Chouteau, 2003).

The IP method is strongly associated with the DC method. It makes use of polarization effects in a low-frequency range that are analogous to a capacitor like reversible storage of energy (Revil et al., 2012). In frequency-domain (FD), mostly a phase shift between transmitter signal and measured voltage is investigated, which is dependent on the transmitter frequency. A special variation of FDIP is the spectral induced polarization (SIP) where several frequencies are employed. Time-domain (TD) applications make use of the voltage decay after transmitter turn-off. Besides information about the subsurface resistivity distribution, the IP method offers the determination

[1] Institute of Geophysics and Meteorology, University of Cologne, Albertus-Magnus-Platz, 50923 Cologne, Germany. E-mail: j.adrian@fz-juelich.de

[2] Institute for Advanced Simulation, IAS-7: Civil Safety Research, Forschungszentrum Jülich, Wilhelm-Johnen-Straße, 52428 Jülich, Germany.

[3] Geophysical Modeling Group (GMG), Department of Geophysical Engineering, Faculty of Engineering, Ankara University, Gölbaşı, 06830 Ankara, Turkey.

Published online: 27 June 2022

of further properties. The most important property is the chargeability which is related to the ability of the subsurface to store energy. Several IP models exist that describe the instant voltage drop and the voltage decay curve after transmitter turn-off.

In the model according to Seigel (1959), the effect of the presence of chargeable material results in an increase of effective resistivity. Other models are e.g. the Cole–Cole model (Pelton, 1977) or the model by Dias (1968), just to name a few. They describe a complex frequency-dependent resistivity. Further parameters such as relaxation time and frequency exponent are introduced allowing to draw conclusions about the texture of the polarizable material. They are represented by an equivalent circuit including a capacitor. Dias (2000) provides an overview of the most commonly used IP models. Effective 2D inversion algorithms for time domain IP data were developed to take into account the whole IP transient (Fiandaca et al., 2013; Hönig & Tezkan, 2007). Besides mineral exploration (Pelton et al., 1978; Seigel et al., 1997; Vanhala & Peltoniemi, 1992), the IP method is also employed for environmental issues, e.g. characterization of contamination of the subsurface (Kemna et al., 2004; Yuval & Oldenburg, 1996), hydrogeological aspects (Hördt et al., 2007; Kemna et al., 2002), investigation of porous rocks and sediments in field surveys (Kemna, 2000; Titov et al., 2004), or laboratory experiments (Bairlein et al., 2014; Zimmermann et al., 2008). A review about recent developments of the DC and the IP method is given in Loke et al. (2013), Revil et al. (2012) and Kemna et al. (2012).

The basis of each inversion algorithm is the implemented forward calculation which serves to create synthetic data for a given subsurface model. In TDIP, commonly the model according to Seigel (1959) is employed, e.g. in the algorithms by Oldenburg and Li (1994), Loke and Barker (1996) or Karaoulis et al. (2013). Then, the synthetic IP datum "apparent chargeability" is derived from DC forward calculation.

In general, most geophysical forward calculations make use of the finite difference (FD) approach (Dey & Morrison, 1979; Mufti, 1976) or the finite element (FE) method (Coggon, 1971). Besides the work of Coggon (1971), further basics of using the FE method for DC problems are presented by Pridmore et al. (1981), Queralt et al. (1991) and Li and Spitzer (2002). The forward problem is to be solved under consideration of boundary conditions that restrict the potential at the boundaries of the computational domain, such as the Neumann boundary condition or mixed boundary conditions (Dey & Morrison, 1979). In FE and FD methods, the computational area is discretized into a grid consisting of mesh elements and nodes. The introduction of boundary elements (Okabe, 1981; Queralt et al., 1991) at the outer mesh boundaries facilitates the incorporation of boundary conditions. Every DC forward problem is eventually reduced to a sparse linear system of equations that is to be solved with respect to the electrical potential.

An overview over efficient solvers is given in Spitzer and Wurmstich (1999). While the FD approach is usually applied on structured rectangular grids, the FE method is suited for the use of unstructured triangular meshes in 2D (Özyıldırım et al., 2020) or tetrahedral grids in 3D (Günther et al., 2006). The advantage of unstructured meshes over structured grids is that local refinement is achieved where accuracy is needed without increasing the number of mesh elements significantly.

Oldenburg and Li (1994) proposed three TDIP inversion approaches. All of them are based on the IP perturbation model according to Seigel (1959), and they recover a resistivity and a chargeability model after two inversion steps. The first step is a DC data inversion recovering a resistivity model. The second step serves to recover a chargeability model. In the first method, the IP data is linearized, and a linear inverse problem is solved under the assumption that chargeability is small. In the second approach, a chargeability model is approximated after two resistivity inversions of perturbed resistivity models. The third method involves a non-linear chargeability inversion.

Several years ago, a copper ore deposit was discovered in Elbistan/Turkey (e.g. Özyildirim et al., 2017; 2020). The ore deposit is assumed to be elongated below the valley. A DC/IP survey was planned and afterwards carried out to derive the lateral and, if possible, vertical borders of the ore body. The DC/TDIP data were observed on eight profiles

perpendicular to the strike direction of the valley. The data should be interpreted with 2D inversion algorithms.

For this study, we developed a new 2D DC/TDIP inversion algorithm (Adrian, 2017) and used it for the 2D inversion of the observed DC/TDIP data from the survey area in Elbistan/Turkey. The algorithm applies a local smoothness constraint regularization approach for 2D inversion of DC and TDIP data including error weighting. The basis of the inversion algorithm is a FE DC forward calculation using unstructured triangular meshes. The inversion procedures are also conducted on an unstructured mesh enabling the incorporation of surface topography. The IP chargeability is determined by a slightly modified version of the third method that was proposed by Oldenburg and Li (1994). It is a non-linear IP inversion subsequent to a non-linear DC inversion. In this approach, there is no need for the chargeability to be small. Therefore, strong and weak chargeability anomalies can be reproduced by the inversion. For more detailed information about the algorithm the reader is referred to Adrian (2017), where modeling studies with synthetic data are also included which test the applicability of the algorithm, and the results are compared with the existing conventional DC/IP algorithms introduced by Günther (2004), Rücker et. al. (2006) and Loke (2002, 2016).

In the following, we introduce the essential features of the applied inversion algorithm and present the inversion results of the DC/TDIP field data. The resulting resistivity models show high resistive structures below low resistive valley sediments, but from the resistivity models alone the presence of an ore body cannot be derived. The chargeability models contain, however, strong IP anomalies with a chargeability of partly more than 100 mV/V, which indicates the presence of the expected disseminated copper ore. From the inversion models, the upper boundary of this structure is clearly seen, but the lower boundary is not revealed by the inversion.

In order to investigate whether the introduction of a lower boundary of the structure followed by low chargeability is realistic, we present a forward modeling study of synthetic data based on an alteration of the chargeability inversion models. It is shown that the datafit can be improved by a lower boundary and a chargeability decrease.

2. *Geological Background of the Survey Area*

The survey area, close to the town of Elbistan, is located in the province of Kahramanmaras in southeastern Turkey. It lies at an altitude of 1170 m to 1200 m above mean sea level in the East Anatolian Fault Zone (Fig. 1) including the Tauride thrust belt where several ophiolitic structures occur (Karaoglan et al., 2013). In general, ophiolitic structures appear in connection with ore deposits (Press & Siever, 2003).

During the collision of the Arabian platform and Anatolia, an oceanic arc of the Neotethys Ocean was partly subsided below the continental crust or was accreted. The accreted material forms the South-East Anatolian Ophiolites which are cropping out along the thrust belt (Kozlu et al., 2014). Since the Göksun Ophiolite (Fig. 1), which lies close to the survey area, belongs to the same tectonic system, it is expected that similar rocks and ore paragenesis are present as they are found at the Isbendere Ophiolite. Near the Isbendere Ophiolite, several sulfide ores were detected in veins and in disseminated form including copper and iron mineralization such as chalcopyrite ($CuFeS_2$), bornite (Cu_5FeS_4), chalcosine (Cu_2S), covelline (CuS), pyrite (FeS_2), sphalerit (ZnS), and marcasite (FeS_2) (Yildirim et al., 2012). The ophiolite is mainly non-metamorph and contains ultramafic–mafic cumulates, isotropic gabbro, a sheeted dyke complex, plagiogranite and volcanic units. Extrusive mafic rocks are exposed e.g. in the Nurhak-Elbistan area. They are comprised of basalt, basaltic andesite, andesite, dacite and rhyolite. Furthermore, volcanic sediments and intercalcations of limestone and mudstone occur.

Generally, the ores are typically found in the oceanic crust where they are formed in hydrothermal deposits at oceanic arcs (Press & Siever, 2003). Where the oceanic crust is subducted beneath the continental crust, ore deposits are found in accreted fragments of the oceanic crust (ophiolites), or they originate from melting and upward intrusion of the subsiding material (Press & Siever, 2003). The

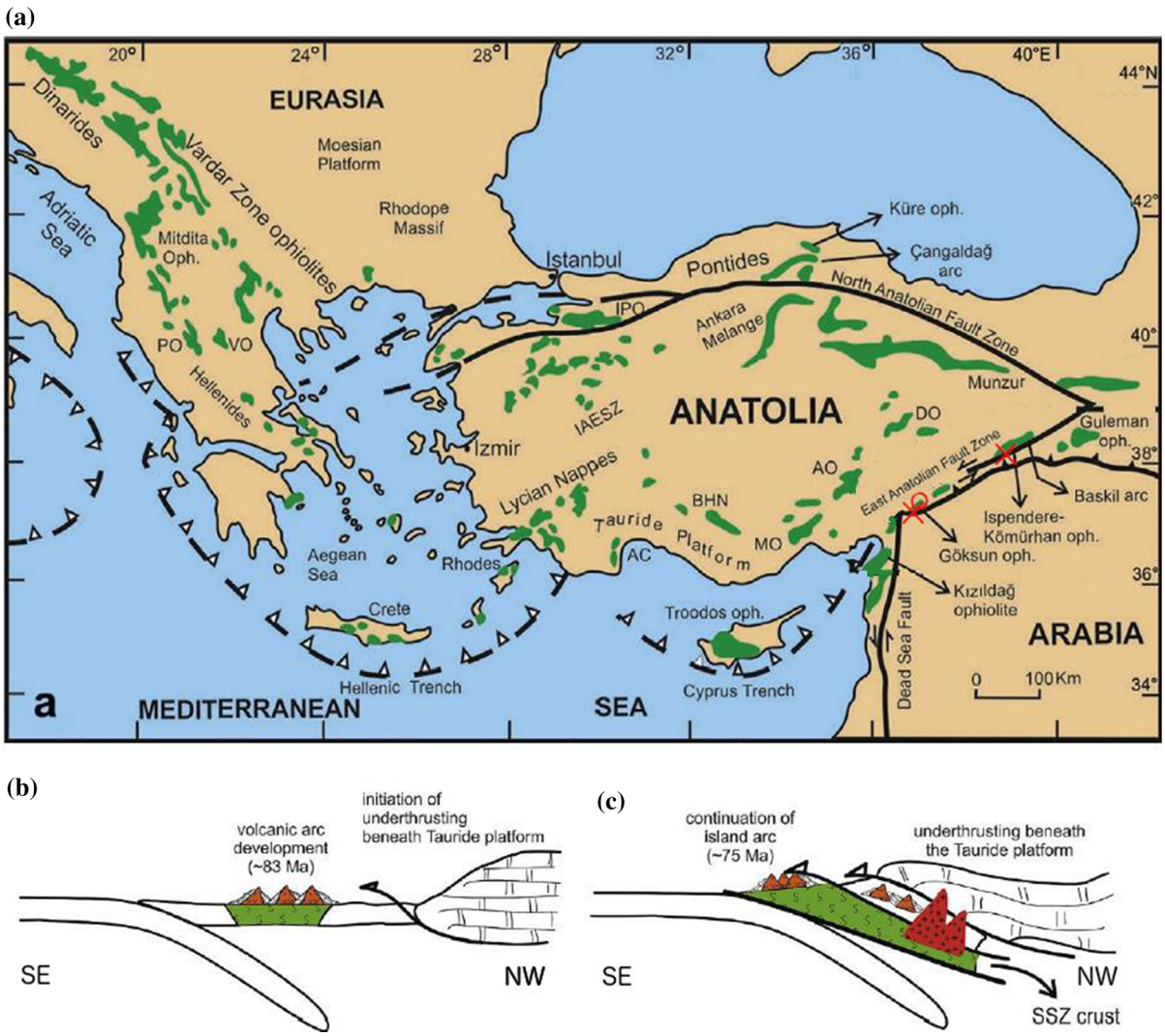


Figure 1

Major tectonic features and distribution of the Neotethyan ophiolites (green) in the eastern Mediterranean region; after Dilek and Flower (2003), Karaoglan et al. (2013). The Survey area is indicated by a red circle, the Göksun and the Isbendere Ophiolite by a red cross, respectively. **b**, **c** Sketch of the development of SSZ-type ophiolites, granitoid intrusions and volcanic sediments, related to the arc, that were subducted or accreted during the late Cretaceous in the northern part of the southern Neotethys (Karaoglan et al., 2013). The sketched subduction is oriented from southeast (SE) to northwest (NW)

deposited ores are then found along veins or are disseminated (finely distributed) within the fractured, intruded material (Press & Siever, 2003; Yildirim et al., 2012).

The survey area covers a copper ore deposit with sulphide being mainly of disseminated form which was discovered several years ago. According to information based on boreholes, the hostrock consists mainly of dacite and copper ore is expected at a depth of more than 8 m below the surface. The ore deposit is assumed to be elongated beneath a valley structure which is oriented approximately from north to south and is flanked by gentle hills (Figs. 2, 3). The valley and the hills are covered by agricultural fields with a dry surface. On the hills, several outcrops of mineralized rocks were observed.

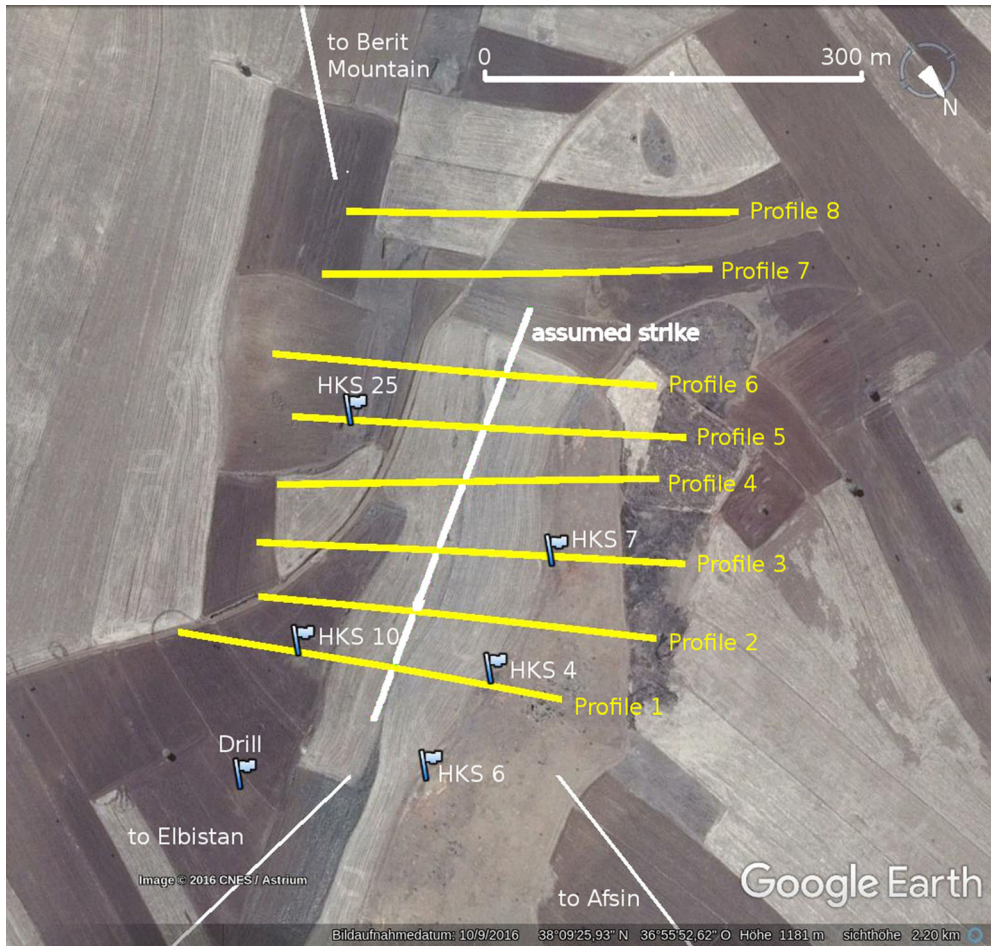


Figure 2
Location of the geophysical profiles (yellow lines) and the assumed strike direction (white line) in the survey area. The north direction is indicated by the compass rose in the upper right corner. Borehole locations are marked by blue symbols. The directions towards the towns of Elbistan and Afsin and the Berit Mountain are indicated as white lines; Google Earth (2016)



Figure 3
Panoramic overview of the survey area in Elbistan: View towards northwestern direction. The white line indicates Profile 3. Borehole locations are labeled with a white cross, the active drilling site by a white circle. Rock outcrops are indicated by a dashed white ellipse

3. Data Acquisition and Measured Data

DC and TDIP data were acquired on eight parallel profiles perpendicular to the valley and the assumed strike direction is as shown in Fig. 2. The total length of each profile was 300 m while the inter-profile distance was around 50 m. A Pole-Dipole configuration was applied with 8 potential electrodes (P1 to P8). The whole setup was moved along the profile. The procedure was done twice, once for a dipole length of a = 10 m and once for a = 20 m. Since eight potential electrodes were used, the acquired data contains seven n-levels for each dipole length with n-spacing of n = 1 to n = 7 (Fig. 4). The largest array spread was 160 m using a dipole length of a = 20 m and an n-spacing of n = 7. Data acquisition was performed using the equipment of Zonge Engineering (Zonge, 2003), namely the transmitter GGT-3 and the receiver GDP32-II with 8 channels. The transmitting signal has a 50% duty cycle and a cycle frequency of f = 0.125 Hz. The measured apparent chargeability is an integrated chargeability given in Newmont Standard (Swift, 1973). The device provides the measured apparent chargeability data in mV/V as an approximation of the Newmont Standard according to (Zonge, 2003): $m_{meas} = s_{zonge} \cdot \frac{T}{1024} \cdot \frac{s_{swift}}{V_p} \cdot \int_{t_1}^{t_2} V_s(t)\mathrm{d}t$, with T = 1/f, $t_1 = 451.38\text{ms}$, $t_2 = 1097.32\text{ms}$, the measured primary voltage V_p, secondary voltage V_s(t), and the internal Zonge constant $s_{\text{zonge}} = 1.53$ (Zonge, 2003). $s_{\text{swift}} = 1.87$ is the swift contant (Swift Jr, 1973).

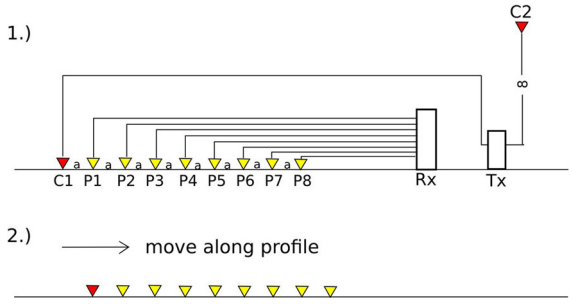


Figure 4
Schematic of the applied Pole-Dipole setup. 1.) The current electrodes C1 and C2 are connected to the Transmitter Tx. Each potential electrode (P1-P8) is connected by a separate cable with the 8-channel receiver Rx. 2.) After each measurement the whole setup is moved along the profile

Data errors were estimated as a sum of a geometry error, voltage error and an additional noise floor of 3%. The geometry error $\left|\frac{\Delta G}{G}\right|$ is the inaccuracy of the geometry factor G used for the calculation of the apparent resistivity and it is based on an electrode displacement which we assume to be $\Delta x \pm 0.15$ m. The voltage error $\left|\frac{\Delta U}{U}\right|$ is based on the inaccuracy of the voltage measurement itself which we estimated to be $\Delta U = \pm 0.5$ mV. Both, geometry and voltage error are dependent on the electrode spread and amount to 2–6% and 0–3%, respectively.

Exemplary for all profiles, the measured data of Profile 3 (Figs. 2, 3) are shown in Fig. 5a,b. The ordinate indicates the n-level in the form a/n. The first n-level refers to a = 10 m and n = 1, which is denoted as 10/1, and the last n-level refers to a = 20 m and n = 7, which is denoted as 20/7. The other 7 profiles show similar pseudo-sections. The measured apparent resistivity values (Fig. 5a) are mainly between 10 and 300 Ωm. The minimum values are found in the first n-levels in the center of the profile and in the last n-levels at the end of the profile. The pseudo-section of the measured apparent resistivities give no clear indication of an ore body. The low resistivities in the center of the valley indicate mainly the near surface valley sediments. On the other hand, the measured apparent chargeabilities (Fig. 5b) are low close to the surface. With growing pseudo-depth, the chargeability increases building two maxima in the beginning and in the center of the profile with values of around 100 mV/V, which can be associated with the ore body (Tezkan & Adrian, 2017).

4. 2D Inversion of the Observed DC/IP Data

The data interpretation was conducted using the 2D DC/TDIP inversion algorithm of Adrian (2017). A brief introduction of this algorithm will be given in the following. A detailed description of the algorithm, including the forward calculation and the comparison of the algorithm using analytical solutions, can be found in (Adrian, 2017). The algorithm applies a smoothness constraint regularization approach with explicit local regularization. For an inversion mesh with N_p elements, the model

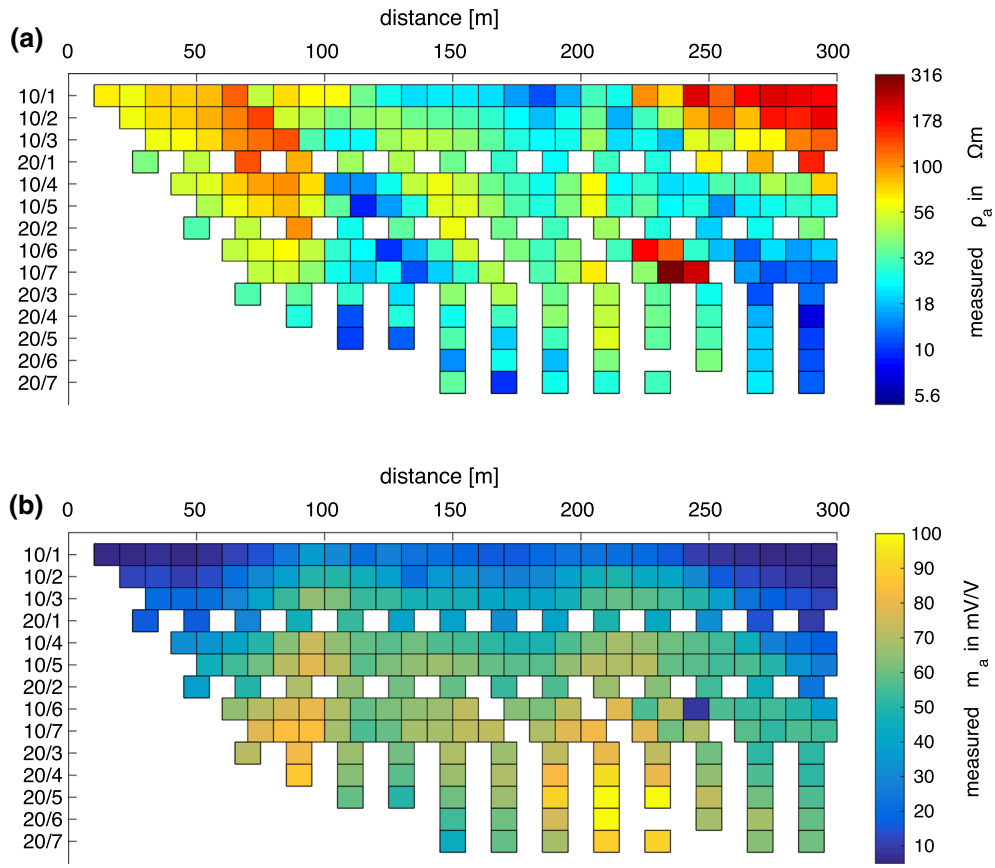


Figure 5
a Apparent resistivity and **b** apparent chargeability measured on Profile 3. The y-axis gives the n-level in the form of a/n

parameter vector is $\boldsymbol{p} = \left(p_1, p_1, \ldots, p_{N_p}\right)^T$. The data vector is $\boldsymbol{d} = (d_1, d_1, \ldots, d_M)^T$ with M data-points and the vector containing data errors is $\boldsymbol{\epsilon} = (\varepsilon_1, \epsilon_1, \ldots, \varepsilon_M)^T$. These vectors contain either resistivity or chargeability parameters. The complete functional Ψ for iteration k reads

$$\Psi = \|\boldsymbol{W}_d\left(\boldsymbol{J}\Delta\boldsymbol{p}^k - \Delta\boldsymbol{d}\right)\|_2^2 + \lambda\|\boldsymbol{C}\Delta\boldsymbol{p}^k\|_2^2 \qquad (1)$$

The left norm in Eq. (1) refers to the data functional Ψ_d. It contains the error weighting matrix $\mathbf{W}_d$ with diagonal entries $1/\varepsilon_m$, the Jacobian or sensitivity matrix, and the model update vector $\Delta\mathbf{p}$. $\boldsymbol{J}$ is the Jacobian or sensitivity matrix with entries $j_{i,j} = \frac{\partial f_m\left(\boldsymbol{p}^k\right)}{\partial p_n^k}$ for the m-th data point $d_m^k = f_m\left(\boldsymbol{p}^k\right)$ and the n-th model parameter p_n^k. The data residual vector $\Delta d = f(p) - d_{meas}$ contains the difference between measured data $\boldsymbol{d}_{meas}$ and the synthetic data according to the model $\boldsymbol{p}$. Since Gaussian noise is expected, a L2-norm is applied.

The second norm in Eq. (1) is the model functional (or stabilizing functional) Ψ_p (Tikhonov & Arsenin, 1977). It regulates the roughness of the model by applying a smoothness constrained matrix $\mathbf{C}$ on the model update $\Delta\mathbf{p}$. Since the smoothness constrained is applied on the model update instead of the model itself, sharp boundaries would be allowed when they are included in the initial model. The smoothness constrained matrix C is a discrete approximation of the partial differential operators (Günther et al., 2006). That means it regulates

changes of model parameters $\Delta\mathbf{p}$ between neighboring elements. For an element i with neighbouring elements n_j (j = 1,2,3), the roughness, which is the inverse of the smoothness, is

$$\begin{aligned} r_i &= (\boldsymbol{C}\Delta\boldsymbol{p})_i \\ &= C_{i,n1}\Delta p_{n1} + C_{i,n2}\Delta p_{n2} + C_{i,n3}\Delta p_{n3} + C_{i,i}\Delta p_i \end{aligned} \tag{2}$$

The simplest case is to set the diagonal entries $C_{i,j} = 3$, the entries $C_{i,nj} = -1$, and the remaining equal to zero. Like this, the contribution of all element boundaries is considered equally. The constraint matrix of this approach is denoted as C_a. To consider different contributions of element vertices according to their varying length and varying element size, the length of the mutual sides L_{nj} and the circumference of the element L_{all} are inserted instead. Then, the entries are $C_{i,nj} = L_{nj}$, $C_{i,I} = -L_{all}$ and 0 else. The corresponding constraint matrix is denoted as C_b.

The functional in Eq. (1) has to me minimised with respect to $\Delta\mathbf{p}$ which leads to

$$\left(\boldsymbol{J}^T\boldsymbol{W}_d^T\boldsymbol{W}_d\boldsymbol{J} + \lambda\boldsymbol{C}^T\boldsymbol{C}\right)\Delta\boldsymbol{p} = \boldsymbol{J}^T\boldsymbol{W}_d^T\boldsymbol{W}_d\Delta\boldsymbol{d} \tag{3}$$

In every iteration k, Eq. (3) is solved using a preconditioned conjugate gradient solver (Freund & Nachtigal, 1996). The result is the model update $\Delta\mathbf{p}^k$. The data-fit χ is determined by

$$\chi = \sqrt{\frac{1}{M}(W_d \cdot \Delta d)^T(W_d \cdot \Delta d)} \tag{4}$$

All forward and inverse calculations are conducted on unstructured meshes facilitating the incorporation of topography.

4.1. Two-Step IP Inversion

As commonly applied in TDIP, the induced polarization is incorporated according to the model of Seigel (1959). In the presence of a non-zero chargeability m, the intrinsic conductivity σ is reduced to an effective conductivity σ':

$$\sigma' = (1-m)\sigma \tag{5}$$

Following this simple relation, synthetic apparent chargeability data m_a can be calculated by double DC forward calculation f_{dc} of the intrinsic and the effective conductivity as:

$$m_a = \frac{f_{dc}(\sigma') - f_{dc}(\sigma)}{f_{dc}(\sigma')} \tag{6}$$

This approach requires an additional forward calculation, but since the computational mesh is the same, the element matrices only need to be calculated once. Thus, the extra computational effort is rather small.

The used algorithm applies a two-step IP inversion approach as proposed by Oldenburg and Li (1994). It assumes that the resistivity model ρ' according to the effective conductivity σ' = 1/ρ' is recovered by the resistivity inversion in the first step. The chargeability model m is obtained by a non-linear chargeability inversion in the second step. In this second step, a resistivity model ρ = 1/σ corresponding to the intrinsic conductivity, is also derived using Eq. (5). This resistivity model ρ is required for the forward calculation according to Eq. (6).

The Jacobian used in the chargeability inversion step can be obtained by simply scaling the DC-sensitivity (Oldenburg & Li, 1994). The partial derivative of the data-point $d_i = m_{a,i}$ with respect to the chargeability of the j-th element yields

$$\frac{\partial d_i}{\partial m_j} = \frac{\Phi_i}{(\Phi_i')^2}\frac{\partial \Phi_i'}{\partial m_j} \tag{7}$$

The potential Φ' is produced by the effective conductivity σ' and Φ by the intrinsic conductivity σ (cf. Equation 6). Under this consideration, $J_{ij}^{dc} = \frac{\partial \Phi_i'}{\partial \sigma_j'}$ is the DC sensitivity and $\frac{\partial \Phi_i'}{\partial m_j} = -\sigma_j J_{ij}^{dc}$. Then, the sought entries of the chargeability sensitivity are obtained from (Oldenburg & Li, 1994)

$$J_{ij}^{ip} = \frac{\partial d_i}{\partial m_j} = -\sigma_j \frac{\Phi_i}{(\Phi_i')^2} J_{ij}^{dc} \tag{8}$$

Different approaches of smoothness constraint matrices were introduced and compared in the 2D inversion algorithm of Adrian (2017). Reasonable results are obtained by the matrix denoted as C_a that

is the general form of the discrete approximation of first order derivatives. However, the employment of the matrix denoted as C_b is recommended because it includes the consideration of the varying length of triangle sides and element areas in the applied unstructured mesh. Moreover, it is shown that the application of a stepwise cooling produces useful results. This procedure starts with the creation of a smooth model by using a rather large regularization parameter in the first inversion iterations. The regularization parameter is only decreased when the data-fit is not decreasing further. This procedure is continued until either the convergence criterion is met or a predefined minimum regularization parameter is reached. Moreover, it was shown that the application of an inexact line-search for an optimum model update step-length in the form of the two-point parabola technique serves to improve convergence and reduce the required number of iterations (Adrian, 2017).

4.2. Coverage and Depth of Investigation

In general, the coverage cov_j or cumulated sensitivity of an element j is obtained by summation of the j-th column of the Jacobian. Obtaining the coverage from summation over $\mathbf{W_d J}$ corresponds to the effect of error weighting (e.g. Martin, 2009). Normalizing the sum with the overall maximum coverage cov_{max} ensures that values of different measurements are comparable because the maximum normalized coverage is always equal to one. Since the sensitivity is dependent on element size, it is reasonable to normalize the coverage additionally with the area of the element A_j yielding

$$\mathrm{cov}_j = \frac{1}{A_j \mathrm{cov}_{max}} \sum_{i=1}^{N} \left| \boldsymbol{W}_{d,ii} \boldsymbol{J}_{ij} \right| \tag{9}$$

The normalization ensures that the coverage of different elements is comparable and independent of discretization and element size. Visualizing the normalized coverage as colour-coded map reveals the sensitivity of the dataset regarding each element's parameter (resistivity or chargeability). Since the sensitivity is influenced by conductivity, the coverage also reacts to conductivity changes. We propose a method to derive a coverage threshold cov_t that approximates a depth of investigation $DOI_{app.}$

Martin (2009) used the coverage to investigate the DOI of transient electromagnetic measurements and applied predefined coverage thresholds to separate well-resolved model domains from poorly resolved domains. Yogeshwar (2014) and Yogeshwar and Tezkan (2017) expanded this method by choosing a threshold based on the coverage of a homogeneous initial model.

For the DC case, we use the DOI according to a rule of thumb DOI_t to derive the threshold cov_t. This estimation is based on sensitivity studies of homogeneous models, and it is dependent on the array type and the array spreading (Barker, 1989). For the largest applied Pole-Dipole spread with a dipole length of $a = 20\,\mathrm{m}$ and a distance between current electrode and first receiving electrode of $a \cdot n = (20\,\mathrm{m}) \cdot 7 = 140\,\mathrm{m}$, the estimated depth according to (Barker, 1989) is $\mathrm{DOI}_t = 0.33 \cdot (a + (a \cdot n)) = 53\,\mathrm{m}$.

The coverage threshold cov_t is derived from the normalized coverage of the initial model which is a homogeneous half-space. The coverage value that coincides with the DOI_t in the center of the profile is defined as cov_t. For the presented survey, the homogeneous initial model has a resistivity of $\rho^0 = 200\ \Omega\mathrm{m}$. In the center of the profile in the depth of $DOI_t = 53$ m, the normalized coverage of the homogeneous half space is $cov_t = 10^{-2.15}$. For the inhomogeneous 2D inversion result (Fig. 6a,b), we use the cov_t -isoline of the corresponding normalized coverage (Fig. 6c,d) as an indication of the approximate $DOI_{app.}$ It separates well resolved from poorly resolved model domains.

4.3. Inversion Results

All inversion results presented in this chapter are derived by the algorithm of Adrian (2017) using the following settings: smoothness matrix C_b, stepwise reduction of the regularization parameter λ, a

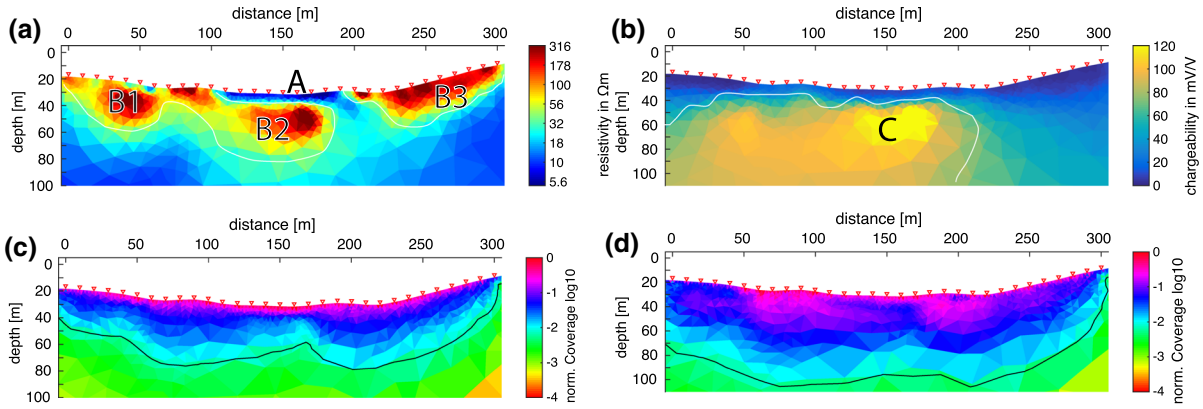


Figure 6

Inversion results Profile 3: **a** Resistivity model, χ_{dc} = 2,5, **b** chargeability model, χ_{ip} = 0,98, **c**, **d** normalized coverage of the corresponding model at the top. Electrode locations are indicated by red triangles. Main structures are delimited by white lines and labelled as A and B1-B3 in the resistivity model and as C in the chargeability model. The approximate DOI_{app} is represented by a black line in the coverage plots

homogeneous initial half space model with ρ^0 = 200 Ωm and m^0 = 10 mV/V, consideration of topography and surface distances.

The resistivity and the chargeability inversion results of Profile 3 are presented in Fig. 6a and b respectively The main structures of the models are labelled as A-C. The corresponding normalised coverage is shown in Fig. 6c,d. Most prominent in the resistivity inversion model (Fig. 6a) is the low resistive structure (A) with less than 15 Ωm and with a thickness of approx. 15 m close to the surface in the centre of the profile which is dipping towards deeper depths at profile distance 200 m. It is followed at depth by a high resistive structure (B2) of > 100 Ωm with a thickness of about 40 m. The near surface resistivity towards the beginning (B1) and the end of the profile (B3) is higher (100–300 Ωm) than in the centre, as was expected from the measured data. The resistivity decreases below the highly resistive structures (B1–B3), which is also supported by a decrease in the measured apparent resistivity in the last n-levels.

The chargeability inversion model (Fig. 6b) shows low chargeability values close to the surface. There is a highly chargeable structure (C) below 20 m depth with a lateral extension of x = 20–200 m and more than 80 mV/V. The maximum chargeability values reach > 100 mV/V and are limited to to x = 130–180 m. A lower boundary of the chargeable structure is not revealed by the inversion model.

From the surface mesh with similar element sizes and for the same electrode setup, the normalized coverage threshold of $10^{-2.15}$, corresponding to the approximate DOI_{app}, was derived. According to the approximate DOI_{app}, the depth of investigation of the resistivity model varies between a depth of 60 m below high resistive structures (B1, B2) and 80 m below low resistive structures to the left and right of the centre. The DOI_{app} corresponding to the chargeability model has a similar form but, according to the sensitivity calculations, is shifted downwards by about 10 m.

The normalized differences displayed in Fig. 7 point out that the data are mostly fitted within the error bounds (within ±1). There are only two outliers visible according to the apparent chargeability. But, for the apparent resistivity, there are several poorly fitted data-points, especially at x = 230–250 m. This shows that the inversion model does not fully reflect the resistivity contrast which is seen in the measured apparent resistivity data in that part of the profile.

Figure 8 shows the 2D inversion results of all eight profiles. The resistivity models (Fig. 8a) vary

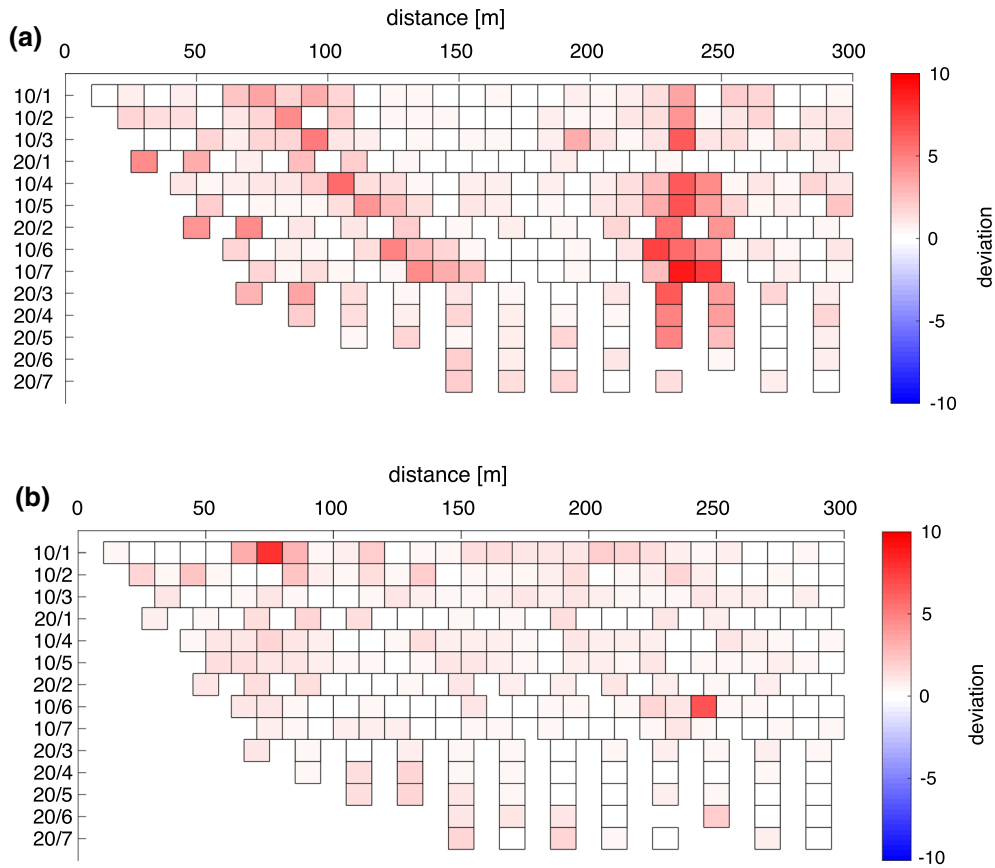


Figure 7
Inversion results of Profile 3: Difference between the measured data and the corresponding calculated data normalized to the data error for **a** the apparent resistivity and **b** the apparent chargeability

from profile to profile, but they have some features in common. The low resistive structure (< 15 m) that lies close to the surface (cf. structure A) appears in all profiles more or less in the centre. It has a thickness of about 15 m. The dipping of this structure towards the bottom right is most prominent in Profile 3. In Profiles 1 and 2, too, there is a connection of the structure to rather low resistivity in deeper depths to the bottom on the right. Below this structure, the resistivity increases. The shape and size of the high resistive structure (cf. structure B2) varies from profile to profile as well as the amplitude of resistivity. All in all, the resistivity of the structure is up to 100–300 Ωm. In most profiles, the structure continues from beneath the low resistive structure towards the beginning of the profiles, i.e. structures B1 and B2 connect. Towards greater depth, it is confined by low resistivities in Profiles 2–5. There is another high resistive structure (B3) of 100–300 Ωm close to the surface at the end of Profiles 1–4. This is where the profiles ascend a hill. The resistivity in this part of the models decreases from Profile 4 to Profile 8 where the resistivity is only approx. 10 Ωm. Profiles 7 and 8 do not ascend this hill and therefore different surface material is expected.

In all chargeability models (Fig. 8b), the chargeability is below 10 mV/V close to the surface, and a highly chargeable structure (cf. structure C) with

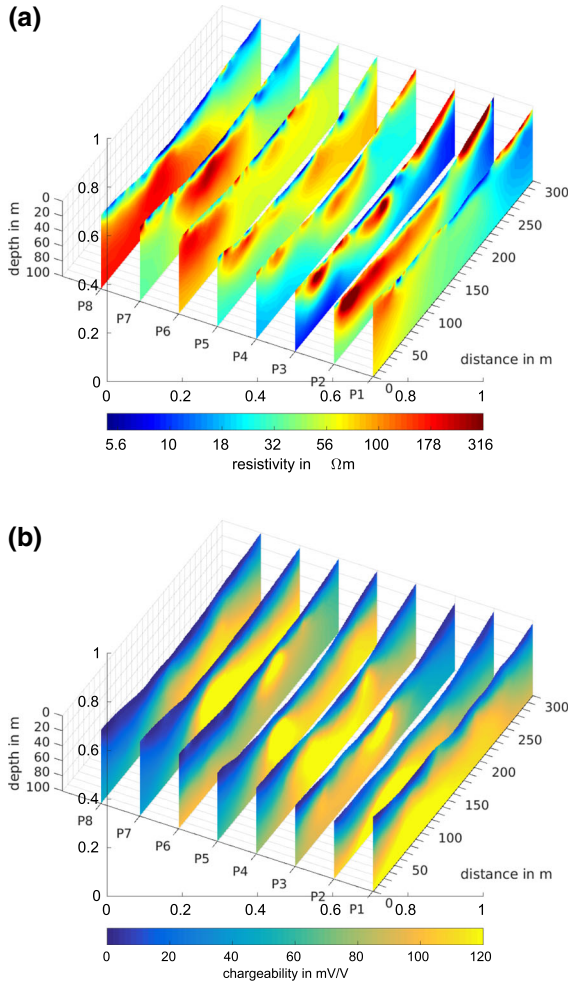


Figure 8
Overview of the inversion results: **a** Resistivity models, **b** Chargeability models

amplitude of more than 100 mV/V appears at depths below approx. 10 m. The main part of this structure seems to be shifted along the x-axis from profile to profile. From that, the strike direction of structure C can be roughly approximated to be oriented from the beginning of Profile 1 to the end of Profile 8 (see sketched strike direction in Fig. 2). In Profile 8, the upper boundary of the structure is lower than in the other profiles and lies close to the approximate DOI.

The presence of the ore deposit is not clearly revealed by the resistivity models alone which is certainly due to its disseminated form. However, the chargeability models show values of partly more than 100 mV/V below a depth of ca. 10 m below the surface. These values indicate the presence of sulfidic ore content. According to the inversion results, the lateral extension can be estimated, and the strike direction of the deposit is roughly oriented from the beginning of Profile 1 to the end of Profile 8. However, the final images do not show a lower boundary of this structure.

By the comparison of the resistivity and chargeability results with borehole information, the obtained physical parameters can be linked to the stratigraphy. Figure 9 shows the inversion models of Profile 1 together with a visualization of borehole information obtained from HKS4 (Fig. 2) which is located at profile distance 250 m. The colours of the borehole stratigraphy refer to resistivity values derived from the inversion results. The dacite layers can be associated with resistivity values of > 200 Ωm for the altered dacite, 50–100 Ωm for the filic dacite and < 50 Ωm for the potassic dacite. These values are, however, in a smaller order of magnitude than the resistivity of dacite listed in (Telford et. al., 1990). A possible explanation is that the texture and composition of the present dacites leads to altered resistivities. According to the simplified geological map of the survey area (Robertson et. al. 2006), the surface layer in the survey area is covered by sediments of the Miocene-Pliocene. This fits to the low resistive surface layer in the centre of the valley. The copper ore content below a depth of 8 m exhibit increased chargeability values of partly > 100 mV/V. According to literature values, a content of 2–8% leads to a significant IP effect. The chargeability increases with a growing sulphide content. Furthermore, copper sulphides chalcocite, chalcopyrite and bornite, and copper produce a significant IP effect even for concentrations of 1%.

4.4. Lower Boundary of the Ore Deposit

The chargeability inversion did not reveal the lower boundary of the highly chargeable structure (C) beneath the investigated 8 profiles using the applied field set-up, at least not within the vertical

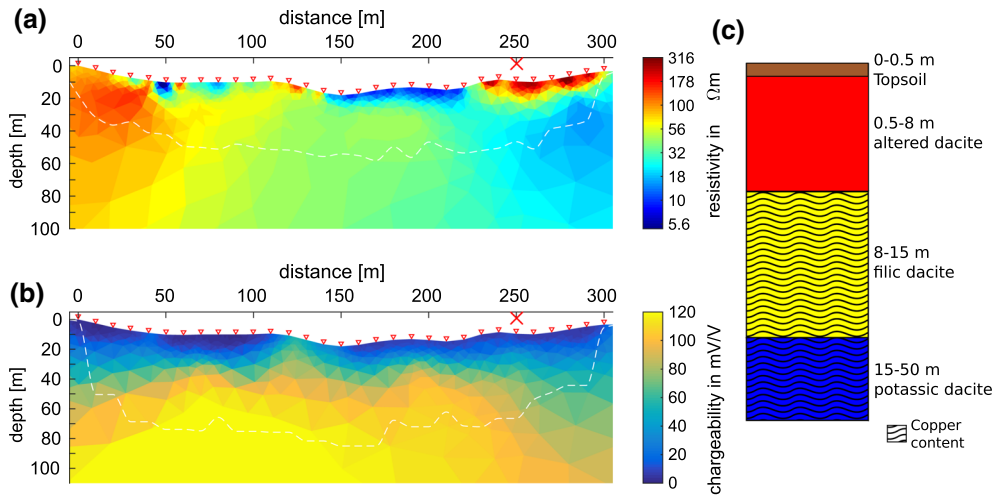


Figure 9

Profile 1: **a** Resistivity (χ_{dc} = 1,6) and **b** chargeability inversion result (χ_{ip} = 0,95). Electrode locations are indicated by red triangles. The dashed white line represents the DOI_{app}. **c** Borehole information obtained from HKS4 (see Fig. 2) located at profile distance 250 m (red cross in a and b)

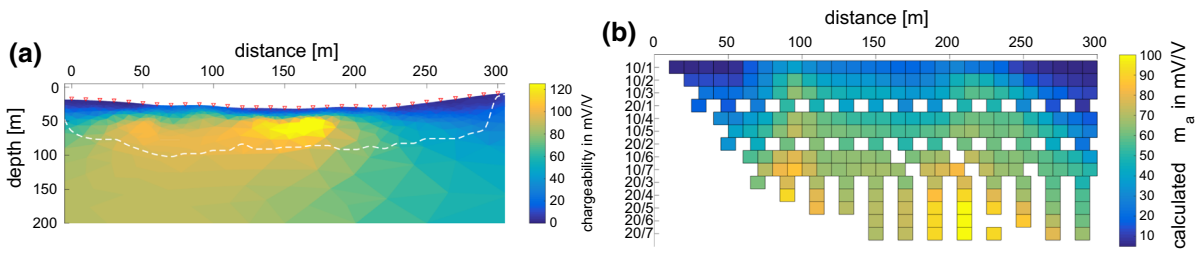
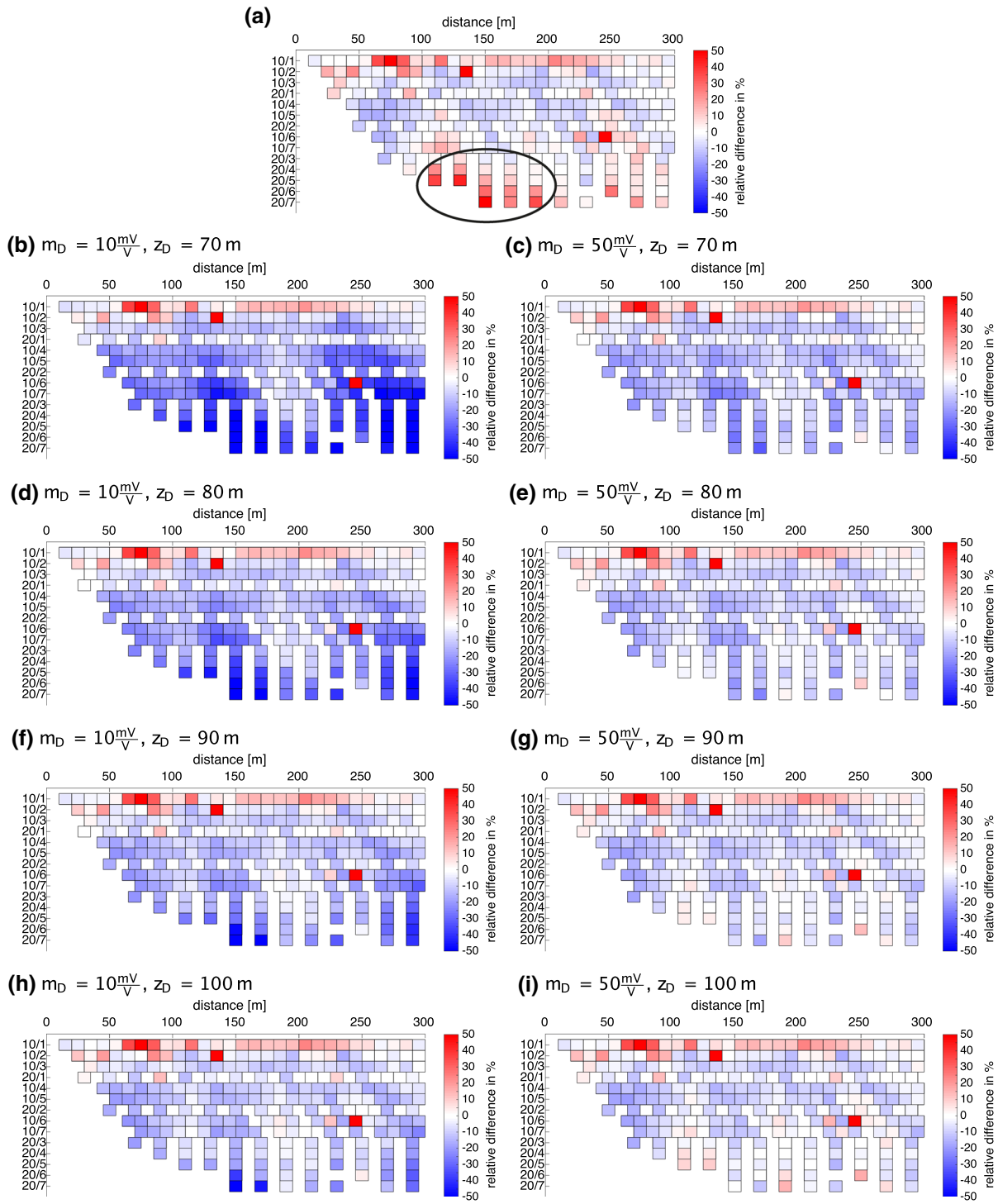


Figure 10

Profile 3: **a** final chargeability inversion result displayed in a depth range from z = 0–200 m, **b** calculated synthetic apparent chargeability data corresponding to the model in (**a**)

extension of the inversion mesh which is, for example, 200 m for profile 3 (Fig. 10). The corresponding calculated synthetic data is shown in Fig. 10b. The data fit for profile 3 (Fig. 7) suggests that the data is fit within the error bounds. In comparison to the original measured data (Fig. 5), the calculated data is mostly similar, which is supported by the data fit. However, the apparent chargeability of the data points at about x = 150 m in the last n-levels (see black ellipse in Fig. 11a) are higher than in the original data. This is emphasized by the relative differences between both data sets shown in Fig. 11a.

To investigate whether the introduction of a chargeability decrease in depth can improve the relative difference, the chargeability model was altered in the following way: Below a certain depth z_D, we introduce a structure D for which the maximum chargeability is set to a certain limit m_D (see Fig. 12 for an example). The resistivity model stays unchanged. Then, a forward calculation of the altered chargeability models is conducted, and the


(a)
distance [m]
0 50 100 150 200 250 300
10/1 10/2 10/3 20/1 10/4 10/5 20/2 10/6 10/7 20/3 20/4 20/5 20/6 20/7
50 40 30 20 10 0 -10 -20 -30 -40 -50
relative difference in %
(b) $m_D = 10\frac{mV}{V}$, $z_D = 70$ m
(c) $m_D = 50\frac{mV}{V}$, $z_D = 70$ m
(d) $m_D = 10\frac{mV}{V}$, $z_D = 80$ m
(e) $m_D = 50\frac{mV}{V}$, $z_D = 80$ m
(f) $m_D = 10\frac{mV}{V}$, $z_D = 90$ m
(g) $m_D = 50\frac{mV}{V}$, $z_D = 90$ m
(h) $m_D = 10\frac{mV}{V}$, $z_D = 100$ m
(i) $m_D = 50\frac{mV}{V}$, $z_D = 100$ m

◀Figure 11
Profile 3: relative difference between measured data and the chargeability data calculated from models including structure D as shown in Fig. 12 with chargeability m_D below z_D. **a** Original inversion result. **b** $m_D = 10\frac{mV}{V}, z_D = 70m, \chi = 1.9$, **c** $m_D = 50\frac{mV}{V}, z_D = 70m, \chi = 1.28$, **d** $m_D = 10\frac{mV}{V}, z_D = 80m, \chi = 1.5$, **e** $m_D = 10\frac{mV}{V}, z_D = 80m, \chi = 1.16$, **f** $m_D = 10\frac{mV}{V}, z_D = 90m, \chi = 1.29$, **g** $m_D = 50\frac{mV}{V}, z_D = 90m, \chi = 1.09$, **h** $m_D = 10\frac{mV}{V}, z_D = 100m, \chi = 1.17$, **i** $m_D = 50\frac{mV}{V}, z_D = 100m, \chi = 1.06$. Here, the data misfit is determined using linear parameters

resulting synthetic data is displayed in terms of relative difference with respect to the measured data (cf. Fig. 11b–i). The left column refers to models in which structure D has a maximum chargeability of m_D = 10 mV/V. This is similar to the values that appear close to the surface. The right column refers to models with a maximum chargeability of structure D of m_D = 50 mV/V which is similar to the values that appear at depths below 50 m in the right part of the chargeability model. The boundary between structures C and D is set to z_D = 70 m in sub-figures (b,c), z_D = 80 m in (d,e), z_D = 90 m in (f,g), and z_D = 100 m in (h,i).

For every altered model, synthetic data was calculated and compared to the measured data. For all tested models with a chargeability maximum of m_D = 10 mV/V, the relative difference indicates that the calculated data is lower than the measured data. The relative difference is influenced from the 3rd n-level downwards. The relative difference according to the models with a chargeability limit of m_D = 50 mV/V in the depth improves in the lower n-levels. The results of the boundary at a depth of z_D = 90 and z_D = 100 m are similar, but the boundary at a depth of 100 m influences the intermediate n-levels less.

According to these model calculations we expect the boundary below structure C at a depth between 90 and 100 m which is slightly below the DOI_{app}. Surely, this investigation is only an approximation, but it reveals that the data-fit of the lower n-levels is improved when a lower boundary with a transition to an intermediate chargeability value is introduced.

5. *Discussion and Conclusion*

We presented the results of a DC/TDIP survey on a copper ore deposit in Turkey. The resistivity model revealed a near surface low resistive structure in the centre of the profile, which implicates the presence of sediments in the trough of the valley. The high resistive structures are presumably associated with mineralized rock with dacite content. This is supported by borehole information and the observation of outcropping rocks on the hill at the end of the profile. Due to the state of the ore deposit, which is mainly disseminated, it was expected that the presence of the metallic particles does not produce a prominent resistivity anomaly. Thus, the deposit is difficult to detect with the DC resistivity method alone. However, the strong induced polarization effects support the hypothesis of a disseminated sulphide content. As expected, highly chargeable structures with more than 100 mV/V are recovered that are associated with the ore deposit. The expansion of the structures is not clearly distinguishable in the resistivity models.

For the modelling of the DC/TDIP field data, the 2D inversion algorithm developed by Adrian (2017) was applied. The algorithm consists of a novel

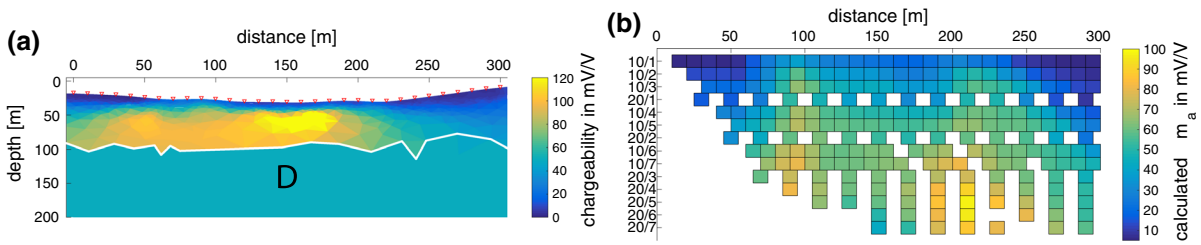


Figure 12
a Chargeability model including structure D with maximum chargeability of mD = 50 mV/V below zD = 100 m. **b** Calculated apparent chargeability corresponding to the model in (**a**)

composition of finite element forward calculation and a smoothness constrained local regularization inversion approach including error weighting and a non-linear IP chargeability inversion. All forward and inverse calculations are conducted on unstructured triangular meshes. The IP chargeability model confines the ore body in the lateral direction, but the lower boundary cannot be identified in the inversion models. By forward modelling of altered models, the location of the boundary is roughly estimated. According to this modelling study, the presence of a boundary at a depth slightly below 90 m improves the data-fit.

Acknowledgements

Part of this research was funded by the Federal Ministry of Education and Research (BMBF, project no: 01DL12028) of Germany and the Scientific and Technological Research Council of Turkey (TÜBİTAK, project no: 110Y343). We thank especially our colleagues at the Department of Geophysical Engineering/Ankara University, Turkey for the collaboration during the field survey and for providing the Zonge equipment.

Author Contributions JA: code development, field measurements, data processing, modelling; BT: supervision of the modelling, field survey, modelling; MEC: field survey, modelling.

Funding

Open Access funding enabled and organized by Projekt DEAL. Part of this research was funded by the Federal Ministry of Education and Research (BMBF, project no: 01DL12028) of Germany and the Scientific and Technological Research Council of Turkey (TÜBİTAK, project no: 110Y343).

Data Availability

The authors confirm that all data and materials as well as software application support their published claims and comply with field standards. The data that support the findings of this study are available from the corresponding author upon reasonable request.

Code Availability

Not applicable.

Declarations

Conflict of Interest The authors have no conflicts of interest to declare that are relevant to the content of this article.

Ethical Approval Not applicable.

Consent to Participate Not applicable.

Consent for Publication The content of the publication is agreed to by all authors.

Open Access This article is licensed under a Creative Commons Attribution 4.0 International License, which permits use, sharing, adaptation, distribution and reproduction in any medium or format, as long as you give appropriate credit to the original author(s) and the source, provide a link to the Creative Commons licence, and indicate if changes were made. The images or other third party material in this article are included in the article's Creative Commons licence, unless indicated otherwise in a credit line to the material. If material is not included in the article's Creative Commons licence and your intended use is not permitted by statutory regulation or exceeds the permitted use, you will need to obtain permission directly from the copyright holder. To view a copy of this licence, visit http://creativecommons.org/licenses/by/4.0/.

Publisher's Note Springer Nature remains neutral with regard to jurisdictional claims in published maps and institutional affiliations.

References

Adrian, J. (2017). Interpretation of DC and IP Time Domain Data Observed on a Copper Deposit in Turkey Using a Newly Developed 2D Finite Element Inversion With Unstructured Meshes. PhD thesis, University of Cologne, Cologne, Germany.

Bairlein, K., Hördt, A., & Nordsiek, S. (2014). The influence on sample preparation on spectral induced polarization of unconsolidated sediments. *Near Surface Geophysics, 12*(5), 667–678. https://doi.org/10.3997/1873-0604.2014023

Barker, R. (1989). Depth of investigation of collinear symmetrical four-electrode arrays. *Geophysics, 54*(8), 1031–1037. https://doi.org/10.1190/1.1442728

Coggon, J. H. (1971). Electromagnetic and electrical modeling by the finite element method. *Geophysics, 36*(1), 132–155. https://doi.org/10.1190/1.1440151

Dey, A., & Morrison, H. F. (1979). Resistivity modelling for arbitrarily shaped two-dimensional structures. *Geophysical Prospecting, 27*(1), 106–136. https://doi.org/10.1111/j.1365-2478.1979.tb00961.x

Dias, C. A. (1968). A non-grounded method for measuring electrical induced polarization and conductivity. PhD thesis, University of California, Berkeley, USA.

Dias, C. A. (2000). Developments in a model to describe low-frequency electrical polarization of rocks. *Geophysics, 65*(2), 437–451. https://doi.org/10.1190/1.1444738

Dilek, Y., & Flower, M. F. (2003). Arc-trench rollback and forearc accretion: 2. a model template for ophiolites in albania, cyprus, and oman. *Geological Society, London, Special Publications, 218*(1), 43–68. https://doi.org/10.1144/GSL.SP.2003.218.01.04

Fiandaca, G., Ramm, J., Binley, A., Gazoty, A., Christiansen, A. V., & Auken, E. (2013). Resolving spectral information from time domain induced polarization data through 2-D inversion. *Geophysical Journal International, 192*(2), 631–646. https://doi.org/10.1093/gji/ggs060

Freund, R. W., & Nachtigal, N. M. (1996). Qmrpack: A package of qmr algorithms. *ACM Transactions on Mathematical Software (TOMS), 22*(1), 46–77. https://doi.org/10.1145/225545.225551

Günther, T. (2004). Inversion Methods and Resolution Analysis for the 2D/3D Reconstruction of Resistivity Structures from DC Measurements. PhD thesis, Freiberg University of Mining and Technology, Germany, available from http://fridolin.tu-freiberg.de. Accessed June 2016

Günther, T., Rücker, C., & Spitzer, K. (2006). Three-dimensional modelling and inversion of dc resistivity data incorporating topography-ii. inversion. *Geophysical Journal International, 166*(2), 506–517. https://doi.org/10.1111/j.1365-246X.2006.03011.x

Hönig, M., & Tezkan, B. (2007). 1D and 2D Cole-Cole Inversion of time domain induced polarization data. *Geophysical Prospecting, 55*, 117–133. https://doi.org/10.1111/j.1365-2478.2006.00570.x

Hördt, A., Blaschek, R., Kemna, A., & Zisser, N. (2007). Hydraulic conductivity estimation from induced polarisation data at the field scale—the Krauthausen case history. *Journal of Applied Geophysics, 62*(1), 33–46. https://doi.org/10.1016/j.jappgeo.2006.08.001

Karaoğlan, F., Parlak, O., Klötzli, U., Koller, F., & Rızaoğlu, T. (2013). Age and duration of intra-oceanic arc volcanism built on a suprasubduction zone type oceanic crust in southern neotethys, se anatolia. *Geoscience Frontiers, 4*(4), 399–408. https://doi.org/10.1016/j.gsf.2012.11.011

Karaoulis, M., Revil, A., Tsourlos, P., Werkema, D. D., & Minsley, B. J. (2013). IP4DI: A software for time-lapse 2D/3D DC-resistivity and induced polarization tomography. *Computers & Geosciences, 54*, 164–170. https://doi.org/10.1016/j.cageo.2013.01.008

Kemna, A. (2000). Tomographic inversion of complex resistivity: theory and application. PhD thesis, Ruhr University Bochum, Germany, Der andere Verlag, Bochum, Germany.

Kemna, A., Binley, A., Cassiani, G., Niederleithinger, E., Revil, A., Slater, L., & Zimmermann, E. (2012). An overview of the spectral induced polarization method for near-surface applications. *Near Surface Geophysics, 10*(6), 453–468. https://doi.org/10.3997/1873-0604.2012027

Kemna, A., Binley, A., & Slater, L. (2004). Crosshole IP imaging for engineering and environmental applications. *Geophysics, 69*(1), 97–107. https://doi.org/10.1190/1.1649379

Kemna, A., Vanderborght, J., Kulessa, B., & Vereecken, H. (2002). Imaging and characterisation of subsurface solute transport using electrical resistivity tomography (ERT) and equivalent transport models. *Journal of Hydrology, 267*(3–4), 125–146. https://doi.org/10.1016/S0022-1694(02)00145-2

Kozlu, H., Prichard, H., Melcher, F., Fisher, P., Brough, C., & Stueben, D. (2014). Platinum group element (pge) mineralisation and chromite geochemistry in the berit ophiolite (elbistan/kahramanmaras), se turkey. *Ore Geology Reviews, 60*, 97–111. https://doi.org/10.1016/j.oregeorev.2013.12.011

Li, Y., & Spitzer, K. (2002). Three-dimensional DC resistivity forward modelling using finite elements in comparison with finite-difference solutions. *Geophysical Journal International, 151*(3), 924–934. https://doi.org/10.1046/j.1365-246X.2002.01819.x

Loke, M. H. (2002). RES2DMOD ver. 3.01. *Rapid 2D resistivity forward modelling using the finite-difference and finite-elements method.* Software Manual. *Geotomo Software*. Malaysia.

Loke, M. H. (2016). RES2DINV version 6.1. Geoelectrical Imaging 2D and 3D. Instruction Manual. Geotomo Software. Malaysia.

Loke, M. H., & Barker, R. D. (1996). Rapid least-squares inversion of apparent resistivity pseudosections by a quasi-Newton method1. *Geophysical Prospecting, 44*(1), 131–152. https://doi.org/10.1111/j.1365-2478.1996.tb00142.x

Loke, M. H., Chambers, J. E., Rucker, D. F., Kuras, O., & Wilkinson, P. B. (2013). Recent developments in the direct-current geoelectrical imaging method. *Journal of Applied Geophysics, 95*, 135–156. https://doi.org/10.1016/j.jappgeo.2013.02.017

Martin, R. (2009). Development and application of 2D and 3D transient electromagnetic inverse solutions based on adjoint Green functions: A feasibility study for the spatial reconstruction of conductivity distributions by means of sensitivities. PhD thesis, University of Cologne, Germany.

Mufti, I. R. (1976). Finite-difference resistivity modeling for arbitrarily shaped two-dimensional structures. *Geophysics, 41*(1), 62–78. https://doi.org/10.1190/1.1440608

Okabe, M. (1981). Boundary element method for the arbitrary inhomogeneities problem in electrical prospecting. *Geophysical Prospecting, 29*(1), 39–59. https://doi.org/10.1111/j.1365-2478.1981.tb01010.x

Oldenburg, D. W., & Li, Y. (1994). Inversion of induced polarization data. *Geophysics, 59*(9), 1327–1341. https://doi.org/10.1190/1.1443692

Özyıldırım, Ö., Candansayar, M. E., Demirci, İ, & Tezkan, B. (2017). Two-dimensional inversion of magnetotelluric/radiomagnetotelluric data by using unstructured mesh. *Geophysics, 82*(4), E197–E210. https://doi.org/10.1190/geo2016-0378.1

Özyıldırım, Ö., Demirci, İ, Gündoğdu, N. Y., & Candansayar, M. E. (2020). Two dimensional joint inversion of direct current resistivity and radiomagnetotelluric data based on unstructured mesh. *Journal of Applied Geophysics, 172*, 103885. https://doi.org/10.1016/j.jappgeo.2019.103885

Pelton, W. H. (1977). Interpretation of induced polarization and resistivity data. PhD thesis, University of Utah, USA.

Pelton, W., Ward, S., Hallof, P., Sill, W., & Nelson, P. H. (1978). Mineral discrimination and removal of inductive coupling with

multifrequency ip. *Geophysics, 43*(3), 588–609. https://doi.org/10.1190/1.1440839

Press, F., & Siever, R. (2003). *Allgemeine Geologie* (3rd ed.). Elsevier.

Pridmore, D. F., Hohmann, G. W., Ward, S. H., & Sill, W. R. (1981). An investigation of finite-element modeling for electrical and electromagnetic data in three dimensions. *Geophysics, 46*(7), 1009–1024. https://doi.org/10.1190/1.1441239

Queralt, P., Pous, J., & Marcuello, A. (1991). 2-D resistivity modeling: An approach to arrays parallel to the strike direction. *Geophysics, 56*(7), 941–950. https://doi.org/10.1190/1.1443127

Revil, A., Karaoulis, M., Johnson, T., & Kemna, A. (2012). Some low-frequency electrical methods for subsurface characterization and monitoring in hydrogeology. *Hydrogeology Journal, 20*(4), 617–658.

Robertson, A. H., Ustaömer, T., Parlak, O., Ünlügenç, U. C., Taşlı, K., & Inan, N. (2006). The Berit transect of the Tauride thrust belt, S Turkey: Late Cretaceous-Early Cenozoic accretionary/collisional processes related to closure of the Southern Neotethys. *Journal of Asian Earth Sciences, 27*(1), 108–145. https://doi.org/10.1016/j.jseaes.2005.02.004

Rücker, C., Günther, T., & Spitzer, K. (2006). Three-dimensional modelling and inversion of dc resistivity data incorporating topography—I. Modelling. *Geophysical Journal International, 166*(2), 495–505. https://doi.org/10.1111/j.1365-246X.2006.03010.x

Seigel, H. O. (1959). Mathematical formulation and type curves for induced polarization. *Geophysics, 24*(3), 547–565. https://doi.org/10.1190/1.1438625

Seigel, H. O., Vanhala, H., & Sheard, S. N. (1997). Some case histories of source discrimination using time-domain spectral ip. *Geophysics, 62*(5), 1394–1408. https://doi.org/10.1190/1.1444244

Spitzer, K., & Chouteau, M. (2003). A dc resistivity and IP borehole survey at the Casa Berardi gold mine in northwestern Quebec. *Geophysics, 68*(2), 453–463. https://doi.org/10.1190/1.1567221

Spitzer, K., & Wurmstich, B. (1999). Speed and accuracy in 3-D resistivity modeling. *Three-dimensional electromagnetics* (pp. 161–176). Society of Exploration Geophysicists. https://doi.org/10.1190/1.9781560802154.ch11

Swift, C., Jr. (1973). The l/m parameter of time-domain ip measurements-a computational analysis. *Geophysics, 38*(1), 61–67. https://doi.org/10.1190/1.1440334

Telford, W. M., Geldart, L. P., & Sheriff, R. E. (1990). *Applied Geophysics* (2nd ed.). Cambridge University Press.

Tezkan, B., & Adrian, J. (2017). A Newly Developed 2D DC and Time-domain IP Inversion Algorithm-Application on Data Acquired on an Ore Deposit in Turkey. *23rd European Meeting of Environmental and Engineering Geophysics*. Vol. 2017. No. 1. European Association of Geoscientists & Engineers. https://doi.org/10.3997/2214-4609.201701979

Tikhonov, A. N., & Arsenin, V. Y. (1977). *Solutions of ill-posed problems*. Winston.

Titov, K., Kemna, A., Tarasov, A., & Vereecken, H. (2004). Induced polarization of unsaturated sands determined through time domain measurements. *Vadose Zone Journal, 3*(4), 1160–1168. https://doi.org/10.2113/3.4.1160

Vanhala, H., & Peltoniemi, M. (1992). Spectral IP studies of Finnish ore prospects. *Geophysics, 57*(12), 1545–1555. https://doi.org/10.1190/1.1443222

Yildirim, N., İlhan, S., Yildirim, E., & Dönmez, C. (2012). The geology, geochemistry and genetical features of the Ormanbaşi Hill (Sincik, Adiyaman) copper mineralization. *Bulletin Mineral Research and Exploration, 144*, 75–104.

Yogeshwar, P. (2014). A resistivity-depth model of the central Azraq basin area, Jordan: 2D forward and inverse modeling of time domain electromagnetic data. PhD thesis, University of Cologne, Germany.

Yogeshwar, P., & Tezkan, B. (2017). Two-dimensional basement modeling of central loop transient electromagnetic data from the central Azraq basin area, Jordan. *Journal of Applied Geophysics, 136*, 198. https://doi.org/10.1016/j.jappgeo.2016.11.001

Yuval, D., & Oldenburg, W. (1996). DC resistivity and IP methods in acid mine drainage problems: Results from the Copper Cliff mine tailings impoundments. *Journal of Applied Geophysics, 34*(3), 187–198. https://doi.org/10.1016/0926-9851(95)00020-8

Zimmermann, E., Kemna, A., Berwix, J., Glaas, W., & Vereecken, H. (2008). EIT measurement system with high phase accuracy for the imaging of spectral induced polarization properties of soils and sediments. *Measurement Science and Technology, 19*(9), 094010. https://doi.org/10.1088/0957-0233/19/9/094010

Zonge (2003). *Zonge GDP-32 II Multifunction Receiver Operation Manual*. Zonge Engineering and Research Organisation Inc., 3322 East Fort Lowell Road, Tucson, AZ 85716 USA

(Received August 18, 2021, revised April 22, 2022, accepted May 14, 2022)